Deep learning illuminates spin and lattice interaction in magnetic materials

Teng Yang,[1,2,*] Zefeng Cai,[2,*] Zhengtao Huang,[1,3,*] Wenlong Tang,[1] Ruosong Shi,[1] Andy Godfrey,[2] Hanxing Liu,[3] Yuanhua Lin,[2] Ce-Wen Nan,[2] Meng Ye,[1] LinFeng Zhang,[4] Ke Wang,[2] Han Wang,[5,6,†] and Ben Xu[1,‡]

[1]*Graduate School of China Academy of Engineering Physics, Beijing 100088, People's Republic of China*

[2]*School of Materials Science and Engineering, Tsinghua University, Beijing 100084, People's Republic of China*

[3]*International School of Materials Science and Engineering, Wuhan University of Technology, Wuhan 430070, People's Republic of China*

[4]*AI for Science Institute, Beijing 100080, People's Republic of China*

[5]*Laboratory of Computational Physics, Institute of Applied Physics and Computational Mathematics, Beijing 100094, People's Republic of China*

[6]*HEDPS, CAPT, College of Engineering, Peking University, Beijing 100871, People's Republic of China*

(Received 12 August 2023; accepted 29 July 2024; published 23 August 2024)

Atomistic simulations hold significant value in clarifying crucial phenomena such as phase transitions and energy transport in materials science. Their success stems from the presence of potential energy functions capable of accurately depicting the relationship between system energy and lattice changes. In magnetic materials, two atomic scale degrees of freedom come into play: the lattice and the spin. However, accurately tracing the simultaneous evolution of both lattice and spin in magnetic materials at an atomic scale is a substantial challenge. This is largely due to the complexity involved in depicting the interaction energy precisely, and its influence on lattice and spin-driving forces, such as atomic forces and magnetic torques, which continues to be a daunting task in computational science. Addressing this deficit, we present DeepSPIN, a versatile approach that generates high-precision predictive models of energy, atomic forces, and magnetic torques in magnetic systems. This is achieved by integrating first-principles calculations of magnetic excited states with deep learning techniques via active learning. We thoroughly explore the methodology, accuracy, and scalability of our proposed model in this paper. Our technique adeptly connects first-principles computations and atomic-scale simulations of magnetic materials. This synergy presents opportunities to utilize these calculations in devising and tackling theoretical and practical obstacles concerning magnetic materials.

DOI: 10.1103/PhysRevB.110.064427

I. INTRODUCTION

Spin-lattice coupling implies that the state of the spin or lattice in a magnetic material system changes in response to changes in the other. This interaction occurs not only in materials with strong spin-orbital coupling (SOC) [1], leading to exotic phenomena such as chirality [2], nonreciprocity [3], superconductivity [4], and quantum criticality [5] but also significantly affects fundamental physical properties, phase transformations [6,7], and transport properties [8] in systems with weak SOC. Simulating this effect computationally is challenging, as it requires accounting for numerous degrees of freedom, high accuracy, and large numbers of simulated atoms. These demands exceed the capabilities of existing first-principles methods, phase-field approaches, micromagnetism, and effective Hamiltonian simulations. Only the recent development of lattice-spin dynamics has shown promise in providing a comprehensive description of these interactions [9–13].

The computational framework for spin-lattice coupling dynamics, originally proposed by Dudarev [14] and Ma [9,10] and later enhanced by Tranchida's implementation in LAMMPS [12], faces a major challenge in accurately describing lattice-spin coupling energies. While machine learning (ML) potentials have proven effective in lattice systems achieving DFT-level accuracy, linear scaling, and broad applicability [15–19], this success has not been mirrored in magnetic materials, despite pioneering efforts by researchers like Nikolov [20], Shapeev [21], and so on [22,23]. Developing accurate ML potentials depends on three key factors: data, model, and data-exploration strategy. However, the complexity of spin interactions and spin-lattice coupling complicates the creation of a comprehensive methodological framework.

First, ground-state-based DFT calculations are unsuitable for generating training data because spin configurations are directly tied to electron distributions, meaning changes in spin states prevent the system from remaining in the ground state. Moreover, temperature or even strain can alter both the spin modulus and direction [24], even in collinear magnetic materials. Consequently, data limited to rotational directions or modulus length changes in collinear configurations are oversimplified for wide-range applications [20,21]. Additionally, magnetic interactions vary across different materials, with no consistent analytical expression for lattice and magnetic

*These authors contributed equally to this work.
†Contact author: wang_han@iapcm.ac.cn
‡Contact author: bxu@gscaep.ac.cn

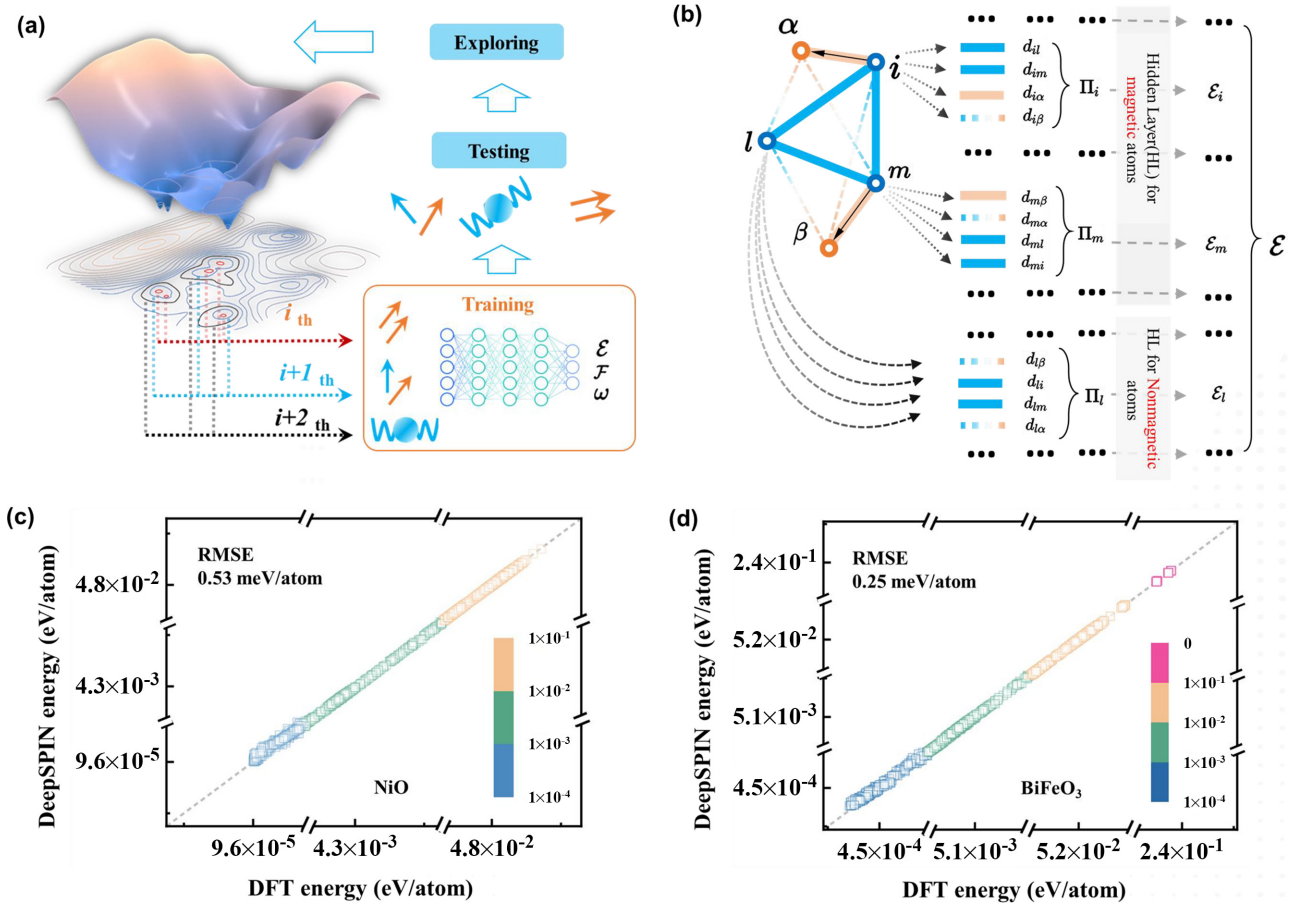

FIG. 1. Active learning diagram to obtain DeepSPIN models. (a) Iterative sampling of the potential energy surface in order of the configuration's energy scale. Each iteration consists of training DeepSPIN models from the current dataset, testing the models' accuracy, and exploring the configuration space for the next energy scale utilizing active learning. (b) Schematic diagram of constructing the DeepSPIN model with pseudoatoms. i, m, and l are real atoms, α and β are pseudoatoms for example. The local environment matrix $\mathbf{\Pi}_i$ consists of the coordinate information from all neighboring atoms and is mapped to atomic energy $\mathcal{E}_i$ by neural networks. [(c) and (d)] The comparisons of energies predicted by DeepSPIN and labeled from DFT on NiO and $BiFeO_3$, respectively. RMSE of predictions is also shown.

interactions, and the magnitude of SOC differing significantly. As a result, manually constructed magnetic Hamiltonians lack universality [20,22]. The energy scales associated with different phenomena also vary widely, so random sampling fails to accurately describe the potential energy surface (PES) that includes both fine-scale events like SOC and large-scale events like atomic displacements. Finally, the complexity of magnetic configurations requires efficient network construction to maximize linear scaling effects, while avoiding complex multilayer function nesting and manual constructions wherever possible [25].

In this work, we address these challenges from three perspectives: data, model, and exploration strategy. To obtain high-precision data for magnetic excited states, we employed a custom-designed self-adaptive constrained method "DeltaSPIN" [26], which acts as a local effective field. By introducing on-the-fly active learning for three special events with different energy scales tailored for magnetic materials, we created a cost-efficient dataset. Additionally, we utilized a "pseudoatom" approach to map the connections between lattice and spin configurations as interdependent features, incorporating a training dataset and a modified loss function that includes magnetic torque. Therefore, in our deep learning model, its accuracy in terms of energy, atomic forces, and magnetic torques has, for the first time, to the best of our knowledge, enabled the study of phase transitions and transport phenomena in magnetic materials and at their interfaces.

We develop a high-precision model capable of accurately describing the potential energy surface $\mathcal{E}(\mathcal{R}, \mathcal{S})$ corresponding to arbitrary lattice configurations $\mathcal{R}$ and spin configurations $\mathcal{S}$. For each magnetic real atom i, we introduce an associated massless "pseudoatom" i^p [e.g., atoms α and β in Fig. 1(b)] around it, representing the spin $\boldsymbol{S}_i$ of atom i through the Cartesian coordinates $\boldsymbol{R}_{i^p}$ of pseudoatom i^p, i.e., $\boldsymbol{R}_{i^p} = \boldsymbol{R}_i + \eta_{\zeta_i} \cdot \boldsymbol{S}_i$. The distance between atom i and pseudoatom i^p is determined by the magnitude of spin $\boldsymbol{S}_i$, multiplied by a scaling factor η_{ζ_i}, ensuring appropriate distance. η_{ζ_i} varies for different element classes. We enumerate all atom indices j satisfying $\|\boldsymbol{r}_{ij}\| < r_c$ (regardless of whether atom j is a real atom or a pseudoatom) to generate a neighbor list $\Omega(i)$ for each real atom i, where $\boldsymbol{r}_{ij} = \boldsymbol{R}_j - \boldsymbol{R}_i$ represents the relative coordinate vector and r_c is the cutoff radius. Following the DeepPot-SE scheme [27,28], we denote the cardinality of $\Omega(i)$ as N_i and construct the local environment matrix $\mathbf{\Pi}_i \in \mathbb{R}^{N_i \times 4}$ for each real atom i, where each row $\boldsymbol{d}_{ij}$ contains the local coordinate

information of the neighboring atom j,

$$\boldsymbol{d}_{ij} = \left\{ \frac{s(r_{ij})}{r_{ij}}, \frac{s(r_{ij})x_{ij}}{r_{ij}^2}, \frac{s(r_{ij})y_{ij}}{r_{ij}^2}, \frac{s(r_{ij})z_{ij}}{r_{ij}^2} \right\}. \quad (1)$$

Here $r_{ij} = \|\boldsymbol{r}_{ij}\|$, x_{ij}, y_{ij}, and z_{ij} are the three components of $\boldsymbol{r}_{ij}$. The smooth factor $s(r_{ij})$ is used to ensure the numerical continuity at the cutoff boundary. It is noteworthy that $\boldsymbol{\Pi}_i$ naturally encompasses three different types of interactions in magnetic systems: lattice-lattice interaction, manifested as the positional relationship between atom i and its neighboring real atoms [e.g., $\boldsymbol{d}_{im}$ in Fig. 1(b)]; lattice-spin interaction, represented by the position relationship between atom i and its neighboring pseudoatoms [e.g., $\boldsymbol{d}_{i\beta}$ in Fig. 1(b)]; and spin-spin interaction, expressed by the position relationship between the pseudoatom i^p and its neighboring pseudoatoms [e.g., $\boldsymbol{d}_{i\alpha}$ and $\boldsymbol{d}_{i\beta}$ in Fig. 1(b)].

Next, we adopt a deep neural network [29] to take each $\boldsymbol{\Pi}_i$ as input and output the corresponding local atomic energy $\mathcal{E}_i$. The neural network comprises two parts [27]: the embedding network, which is a specially designed network that encodes $\boldsymbol{\Pi}_i$ into high-dimensional feature vectors preserving the system's translational, rotational, and permutation symmetries; and the fitting network, which is a fully connected residual network [30] that maps the obtained feature vectors to $\mathcal{E}_i$. The network parameters corresponding to each element type are independent of each other and shared among all atoms belonging to that type. The total energy $\mathcal{E}$ of the system is expressed as the sum of atomic energies $\mathcal{E}_i$ for all N real atoms, i.e., $\mathcal{E} = \sum_i^N \mathcal{E}_i$, thereby preserving the extensive character.

The atomic force $\mathcal{F}_i$ can be analytically expressed as the derivative of $\mathcal{E}$ with respect to the atomic position $\boldsymbol{R}_i$ and expanded by the chain rule, as shown in Eq. (2), where $\Omega_r(i)$ represents all neighboring real atoms of atom i. Since the position $\boldsymbol{R}_i$ and the corresponding pseudoatom position $\boldsymbol{R}_{i^p}$ jointly affect $\mathcal{E}_j$, we introduce the coefficient δ_i to distinguish the magnetism of atoms, i.e., $\delta_i = 1$ for magnetic atoms and $\delta_i = 0$ otherwise. Similarly, the magnetic torque ω_i can be expressed as the derivative of $\mathcal{E}$ with respect to the spin $\boldsymbol{S}_i$, as shown in Eq. (3). Here $\boldsymbol{S}_i$ affects $\mathcal{E}_j$ through the pseudoatom position $\boldsymbol{R}_{i^p}$. In this way, both atomic forces and magnetic torques are influenced by real and pseudo atoms,

$$\begin{aligned}
\mathcal{F}_i &= -\frac{\partial \mathcal{E}}{\partial \boldsymbol{R}_i} = -\sum_k^N \frac{\partial \mathcal{E}_k}{\partial \boldsymbol{\Pi}_k} \cdot \frac{\partial \boldsymbol{\Pi}_k}{\partial \boldsymbol{R}_i} \\
&= -\sum_{j\in\Omega(i)} \frac{\partial \mathcal{E}_i}{\partial \boldsymbol{d}_{ij}} \cdot \frac{\partial \boldsymbol{d}_{ij}}{\partial \boldsymbol{R}_i} \\
&\quad + \sum_{j\in\Omega_r(i)} \left\{ \frac{\partial \mathcal{E}_j}{\partial \boldsymbol{d}_{ji}} \cdot \frac{\partial \boldsymbol{d}_{ji}}{\partial \boldsymbol{R}_j} + \delta_i \cdot \frac{\partial \mathcal{E}_j}{\partial \boldsymbol{d}_{ji^p}} \cdot \frac{\partial \boldsymbol{d}_{ji^p}}{\partial \boldsymbol{R}_j} \right\}, \quad (2)
\end{aligned}$$

$$\begin{aligned}
\omega_i &= -\frac{\partial \mathcal{E}}{\partial \boldsymbol{S}_i} = -\sum_k^N \frac{\partial \mathcal{E}_k}{\partial \boldsymbol{\Pi}_k} \cdot \frac{\partial \boldsymbol{\Pi}_k}{\partial \boldsymbol{R}_{i^p}} \cdot \frac{\partial \boldsymbol{R}_{i^p}}{\partial \boldsymbol{S}_i} \\
&= \left\{ \frac{\partial \mathcal{E}_i}{\partial \boldsymbol{d}_{ii^p}} \cdot \frac{\partial \boldsymbol{d}_{ii^p}}{\partial \boldsymbol{R}_i} + \sum_{j\in\Omega_r(i)} \frac{\partial \mathcal{E}_j}{\partial \boldsymbol{d}_{ji^p}} \cdot \frac{\partial \boldsymbol{d}_{ji^p}}{\partial \boldsymbol{R}_j} \right\} \cdot \eta_{\zeta_i}. \quad (3)
\end{aligned}$$

To efficiently train the neural network, we design the loss function in the form of Eq. (4), where Δ represents the difference between the DeepSPIN prediction and the label, N and N_s represent the number of real atoms and pseudoatoms respectively, and $p_\mathcal{E}$, $p_\mathcal{F}$, and p_ω are adjustable weights controlling the contributions of atomic energy, atomic forces, and magnetic torques in the loss function, respectively. We employ the Adam optimizer [31] to minimize the loss function, ensuring accurate predictions for each component and achieving faster training speed,

$$\begin{aligned}
&\mathcal{L}(p_\mathcal{E}, p_\mathcal{F}, p_\omega) \\
&= p_\mathcal{E}\left(\frac{\Delta\mathcal{E}}{N}\right)^2 + \frac{p_\mathcal{F}}{3N}\sum_i^N \|\Delta\mathcal{F}_i\|^2 + \frac{p_\omega}{3N_s}\sum_i^{N_s} \|\Delta\omega_i\|^2.
\end{aligned} \quad (4)$$

Moreover, to obtain high-precision labels, we perform first-principles calculations on noncollinear magnetic configurations using the DeltaSpin scheme [26]. DeltaSpin optimizes the Lagrangian function $\mathcal{L}[\rho; \{\boldsymbol{\lambda}_i, \boldsymbol{S}_i, \boldsymbol{S}_i^*\}] = E_{\mathrm{KS}}[\rho] - \sum_i \boldsymbol{\lambda}_i \cdot (\boldsymbol{S}_i[\rho] - \boldsymbol{S}_i^*)$, which can lead to the errors of magnetic moments and energy converging to $\delta\boldsymbol{S} = 10^{-5}$ μ_B and $\delta\mathcal{E} = 10^{-9}$ eV, respectively. In this approach, magnetic torque ω_i can be obtained using a method similar to the Hellman-Feynman scheme [32], i.e., $\omega_i = -\delta\mathcal{L}/\delta\boldsymbol{S}_i^* = -\boldsymbol{\lambda}_i$.

Using an active learning strategy [33,34], we explore the configuration space of lattice and spin from the magnetic ground state, constructing the PES [shown in Fig. 2(a)]. These

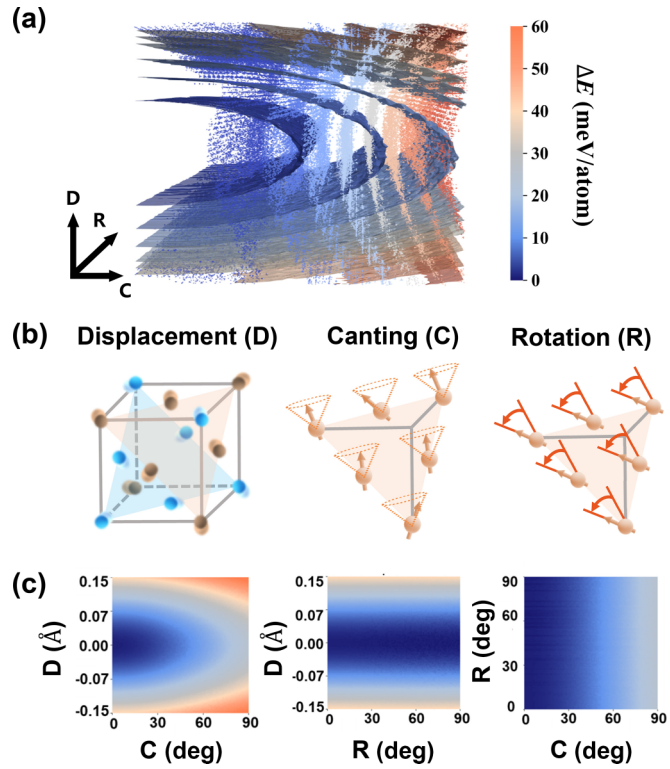

FIG. 2. Profiles of high dimensional potential energy surface (PES). (a) Three-dimensional PES of NiO constructed with respect to diverse physical events, varying colors represent different energy scale relative to the ground state. (b) Illustrations of three pertubative events as D, C, and R. (c) Projections of PES along each axis, offering the quantitative assessment of energy from different pertubations.

events perturb real atom positions (displacement, D), change spin orientations (canting, C), or simultaneously rotate all spins (rotation, R). Figure 2(b) visually demonstrates these in a primitive cell of NiO, where D is limited to position changes along the Ni-Ni line with one Ni atom stationary, and the C axis reflects angle changes after fixing one Ni atom's spin and perturbing the other's. Iterative sampling and model training enrich the dataset, filtering configurations based on certain thresholds. Model parameters are tuned iteratively, gradually increasing upper limits for physical events (see the Supplemental Material [35]).

We highlight the efficacy of DeepSPIN method through studies on two antiferromagnetic insulating materials: NiO and $BiFeO_3$. NiO exhibits stable antiferromagnetic order with minimal magnetic anisotropy [47–49]. In contrast, $BiFeO_3$ is a multiferroic system characterized by pronounced Dzyaloshinskii-Moriya (DM) interactions, embodying a complex interplay between oxygen octahedral rotations and subdued ferromagnetic moments [50–53]. Figures 1(c) and 1(d) depict a compelling agreement between the energies predicted by the DeepSPIN model and those derived from DFT for excited states. Notably, the distribution of average relative atomic energy spans four orders of magnitude from 10^{-4} eV to 10^{-1} eV, represented by varying colors, underscoring the model's impressive accuracy. In Fig. 2(c), we present the delineated potential energy surface profiles for three unique physical events. This visualization allows for nuanced evaluations of energy associated with various excitation modes. Figures 3(c) and 3(d) further showcase the model's proficiency in predicting atomic forces and magnetic torques, registering RMSE values of 5.9 meV/μB and 7.7 meV/Å, respectively. The precise torque predictions can be seamlessly integrated into frameworks like time-dependent DFT [54,55] or Landau-Lifshitz-Gilbert equations [56], serving as primary drivers for spin evolution.

The DeepSPIN model can also reveal the influence of spin-lattice interaction on the dynamic properties of magnetic systems, such as phonon spectra and magnon spectra [57–59]. Figures 3(a) and 3(b) illustrate the impact of varying magnetic configuration on lattice dynamics. When the magnetic configuration of NiO changes from the antiferromagnetic ground state (G-state) to mutually orthogonal excited states (R-state), as shown in Fig. 3(c), acoustic branches of the phonon spectrum remain nearly unchanged, while the frequencies of the optical branches undergo significant variations with magnitude close to 3 meV. This reflects the distinct interactions between magnetic Ni atoms within or between the {111} plane as well as the superexchange interaction along the Ni-O-Ni chain [48]. Moreover, the impact of lattice configurations on spin dynamics can be also revealed (see Fig. S4 in the Supplemental Material [35]). When −3% uniform compressive strain is applied to $R3c$ $BiFeO_3$, the magnon frequency increases significantly, indicating enhanced magnetic interactions and greater stability of the antiferromagnetic order. The comparison of the spectra obtained from DeepSPIN with DFT calculations highlights the accuracy of the DeepSPIN model.

DeepSPIN demonstrates superior generalizability in various application scenarios. We construct a high-angle NiO grain boundary system (Σ5) with mirror-symmetric atomic

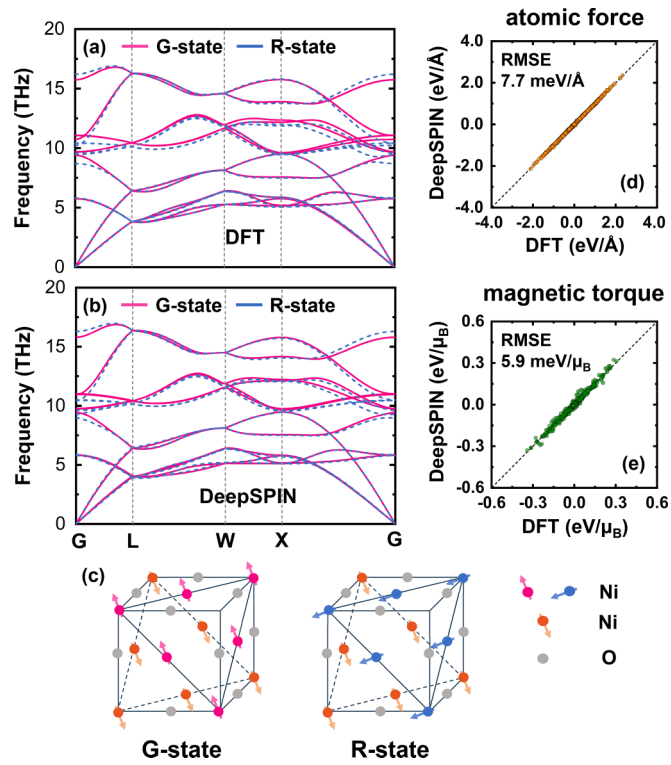

FIG. 3. Validating predictions of spin-lattice coupling via lattice dynamics analysis. [(a) and (b)] The comparisons of NiO phonon spectra of G-state (red) and R-state (blue) configuration, obtained from DFT and DeepSPIN, respectively. (c) Illustrations of G-state and R-state, representing in-plane spin rotation of Ni atoms. [(d) and (e)] Comparisons of atomic forces and magnetic torques predicted by DeepSPIN and labeled from DFT, respectively. RMSE is shown.

distribution on both sides of the grain boundary $(\overline{3}10)$ [60]. All Ni atoms are initially set to antiferromagnetic ground state. The system contains 11,328 atoms in total and has dimensions of 8, 1.6, and 7.7 nm along three directions, exceeding the affordable scale of first-principles calculations. Figures 4(a) and 4(b) illustrate the optimization results of the spin configuration by the DeepSPIN model. The Ni atoms maintain the $\langle 11\overline{2}\rangle$ antiferromagnetic order away from the grain boundary but exhibit highly irregular distorted configurations near the boundary, resulting in local net magnetic moments, consistent with previous studies [61]. Additionally, we apply the nudge elastic band method [62,63] to calculate the 180° polarization switching process of $R3c$ $BiFeO_3$ along the [111] direction [64]. As shown in Fig. 4(c), DeepSPIN model not only successfully obtains the energy barrier for polarization switching but also accurately predicts the energy of the distorted structures along the switching trajectory [65]. This indicates DeepSPIN is effectively capable of capturing the complex spin-lattice interaction involving Bi displacements and FeO_6 oxygen octahedral distortions, and even potentially can address dynamic magnetoelectricity [66].

In conclusion, we propose a flexible approach to derive spin-lattice coupling models, which facilitates the construction of deep neural networks for magnetic materials' energy, atomic forces, and magnetic torques. This method outperforms other electronic and mesoscale techniques when

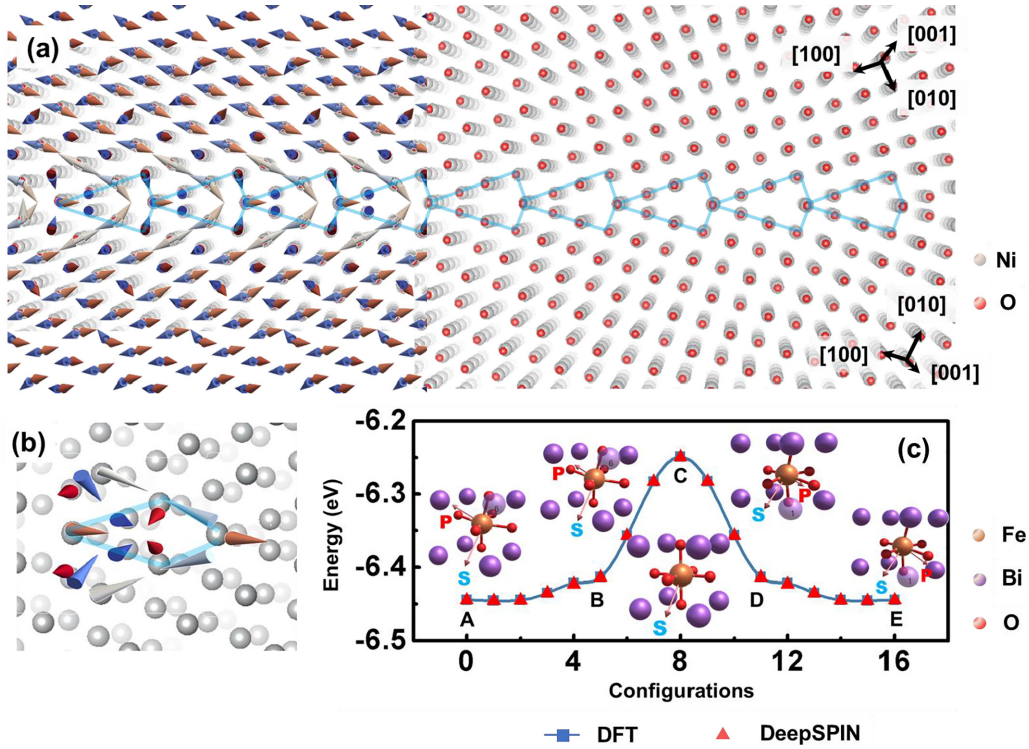

FIG. 4. Predictions of spin-lattice coupling in complex crystal structures. (a) The optimized spin configuration within Σ5 symmetric NiO grain boundary (left side) and the crystal structure obtained from high-resolution electron microscopy [60] (right side). (b) Enlarged view of the local Ni spin distribution on the grain boundaries. Varying colors represent the magnitude of the y axis ([112]) component. Red and blue correspond to the maximum values in the [112] and $[\bar{1}\bar{1}\bar{2}]$ directions, respectively. (c) Energy barrier derived from DFT and DeepSPIN for the 180° polarization switching trajectory in $BiFeO_3$ with varying polarization $\boldsymbol{P}$ and fixed magnetization $\boldsymbol{S}$. The modulus of P gradually diminishes to 0 and then increases inversely.

dealing with various magnetic and crystal structures, especially those exhibiting significant irregularities in lattice and spin arrangements. DeepSPIN notably maintains high accuracy even when the average atomic energy reaches 10^{-4} eV, atomic forces below 10 meV/Å, and magnetic torques below 10 meV/μ_B. Although the "curse of dimensionality" requires a relatively large dataset in configuration space to achieve the aforementioned accuracy, this difficulty can be mitigated by the active learning scheme. Through integrating DeepSPIN with atomic-scale spin-lattice dynamics techniques, we are now equipped to address various phenomena, such as paramagnetic states, phonon-magnon interactions, and even quantum critical phenomena in magnetic materials when quantum thermobath is applied.

ACKNOWLEDGMENTS

B.X. acknowledges the support of the National Natural Science Foundation of China (NSFC, Grant No. 52072209), the Basic Science Center Program of the National Natural Science Foundation of China (Grant No. U2330401).

[1] V. Baltz, A. Manchon, M. Tsoi, T. Moriyama, T. Ono, and Y. Tserkovnyak, Antiferromagnetic spintronics, Rev. Mod. Phys. **90**, 015005 (2018).

[2] C. Liu, W. Ren, and S. Picozzi, Spin-chirality-driven multiferroicity in van der Waals monolayers, Phys. Rev. Lett. **132**, 086802 (2024).

[3] T. Nomura, X.-X. Zhang, R. Takagi, K. Karube, A. Kikkawa, Y. Taguchi, Y. Tokura, S. Zherlitsyn, Y. Kohama, and S. Seki, Nonreciprocal phonon propagation in a metallic chiral magnet, Phys. Rev. Lett. **130**, 176301 (2023).

[4] C. B. Bishop, A. Moreo, and E. Dagotto, Bicollinear antiferromagnetic order, monoclinic distortion, and reversed resistivity anisotropy in FeTe as a result of spin-lattice coupling, Phys. Rev. Lett. **117**, 117201 (2016).

[5] A. Narayan, A. Cano, A. V. Balatsky, and N. A. Spaldin, Multiferroic quantum criticality, Nat. Mater. **18**, 223 (2019).

[6] L. Vitos, P. A. Korzhavyi, and B. Johansson, Evidence of large magnetostructural effects in Austenitic stainless steels, Phys. Rev. Lett. **96**, 117210 (2006).

[7] R. Singer, F. Dietermann, and M. Fähnle, Spin interactions in bcc and fcc Fe beyond the Heisenberg model, Phys. Rev. Lett. **107**, 017204 (2011).

[8] I. Stockem, A. Bergman, A. Glensk, T. Hickel, F. Körmann, B. Grabowski, J. Neugebauer, and B. Alling, Anomalous phonon lifetime shortening in paramagnetic CrN caused by spin-lattice coupling: A combined spin and ab initio molecular dynamics study, Phys. Rev. Lett. **121**, 125902 (2018).

[9] P.-W. Ma, C. H. Woo, and S. L. Dudarev, Large-scale simulation of the spin-lattice dynamics in ferromagnetic iron, Phys. Rev. B **78**, 024434 (2008).

[10] P.-W. Ma, S. Dudarev, and C. Woo, SPILADY: A parallel CPU and GPU code for spin–lattice magnetic molecular dynamics simulations, Comput. Phys. Commun. **207**, 350 (2016).

[11] D. Perera, D. M. Nicholson, M. Eisenbach, G. M. Stocks, and D. P. Landau, Collective dynamics in atomistic models with coupled translational and spin degrees of freedom, Phys. Rev. B **95**, 014431 (2017).

[12] J. Tranchida, S. J. Plimpton, P. Thibaudeau, and A. P. Thompson, Massively parallel symplectic algorithm for coupled magnetic spin dynamics and molecular dynamics, J. Comput. Phys. **372**, 406 (2018).

[13] P. Chen, H. Zhao, S. Artyukhin, and L. Bellaiche, LINVARIANT, https://github.com/PaulChern/LINVARIANT.

[14] S. Dudarev and P. Derlet, A 'magnetic' interatomic potential for molecular dynamics simulations, J. Phys.: Condens. Matter **17**, 7097 (2005).

[15] A. P. Bartók, M. C. Payne, R. Kondor, and G. Csányi, Gaussian approximation potentials: The accuracy of quantum mechanics, without the electrons, Phys. Rev. Lett. **104**, 136403 (2010).

[16] A. P. Bartók, R. Kondor, and G. Csányi, On representing chemical environments, Phys. Rev. B **87**, 184115 (2013).

[17] K. T. Schütt, H. E. Sauceda, P.-J. Kindermans, A. Tkatchenko, and K.-R. Müller, Schnet–a deep learning architecture for molecules and materials, J. Chem. Phys. **148**, 241722 (2018).

[18] L. Zhang, J. Han, H. Wang, R. Car, and W. E, Deep potential molecular dynamics: A scalable model with the accuracy of quantum mechanics, Phys. Rev. Lett. **120**, 143001 (2018).

[19] L. Zhang, H. Wang, R. Car, and W. E, Phase diagram of a deep potential water model, Phys. Rev. Lett. **126**, 236001 (2021).

[20] S. Nikolov, M. A. Wood, A. Cangi, J.-B. Maillet, M.-C. Marinica, A. P. Thompson, M. P. Desjarlais, and J. Tranchida, Data-driven magneto-elastic predictions with scalable classical spin-lattice dynamics, npj Comput. Mater. **7**, 153 (2021).

[21] I. Novikov, B. Grabowski, F. Körmann, and A. Shapeev, Magnetic Moment Tensor Potentials for collinear spin-polarized materials reproduce different magnetic states of bcc Fe, npj Comput. Mater. **8**, 13 (2022).

[22] M. Domina, M. Cobelli, and S. Sanvito, Spectral neighbor representation for vector fields: Machine learning potentials including spin, Phys. Rev. B **105**, 214439 (2022).

[23] P. Zhang and G.-W. Chern, Machine learning nonequilibrium electron forces for spin dynamics of itinerant magnets, npj Comput. Mater. **9**, 32 (2023).

[24] M. van Schilfgaarde, I. A. Abrikosov, and B. Johansson, Origin of the Invar effect in iron–nickel alloys, Nature (London) **400**, 46 (1999).

[25] M. Rinaldi, M. Mrovec, A. Bochkarev, Y. Lysogorskiy, and R. Drautz, Non-collinear magnetic atomic cluster expansion for iron, npj Comput. Mater. **10**, 12 (2024).

[26] Z. Cai, K. Wang, Y. Xu, S.-H. Wei, and B. Xu, First-principle study of magnetic excitation by using self-adaptive spin-constrained DFT, Quantum Front. **2**, 21 (2023).

[27] L. Zhang, J. Han, H. Wang, W. Saidi, R. Car, and W. E, End-to-end symmetry preserving inter-atomic potential energy model for finite and extended systems, in *Advances in Neural Information Processing Systems* (Curran Associates, Inc., New York, 2018), Vol. 31.

[28] H. Wang, L. Zhang, J. Han, and W. E, DeePMD-kit: A deep learning package for many-body potential energy representation and molecular dynamics, Comput. Phys. Commun. **228**, 178 (2018).

[29] I. J. Goodfellow, Y. Bengio, and A. Courville, *Deep Learning* (MIT Press, Cambridge, MA, 2016).

[30] K. He, X. Zhang, S. Ren, and J. Sun, Deep residual learning for image recognition, in *Proceedings of the IEEE Conference on Computer Vision and Pattern Recognition (CVPR'16)* (IEEE, New York, 2016).

[31] D. P. Kingma and J. Ba, Adam: A method for stochasticoptimization, arXiv:1412.6980 [cs.LG].

[32] R. P. Feynman, Forces in molecules, Phys. Rev. **56**, 340 (1939).

[33] L. Zhang, D.-Y. Lin, H. Wang, R. Car, and W. E, Active learning of uniformly accurate interatomic potentials for materials simulation, Phys. Rev. Mater. **3**, 023804 (2019).

[34] Y. Zhang, H. Wang, W. Chen, J. Zeng, L. Zhang, H. Wang, and W. E, DP-GEN: A concurrent learning platform for the generation of reliable deep learning based potential energy models, Comput. Phys. Commun. **253**, 107206 (2020).

[35] See Supplemental Material at http://link.aps.org/supplemental/10.1103/PhysRevB.110.064427 for details of first-principles calculations; model framework, parameters tuning, model training and dataset construction of DeepSPIN models; model performance on datasets; magnon spectra of $BiFeO_3$; and spin-lattice atomistic simulations, which also includes Refs. [36–46].

[36] G. Kresse and J. Hafner, *Ab initio* molecular-dynamics simulation of the liquid-metal–amorphous-semiconductor transition in germanium, Phys. Rev. B **49**, 14251 (1994).

[37] G. Kresse and J. Furthmüller, Efficiency of ab-initio total energy calculations for metals and semiconductors using a plane-wave basis set, Comput. Mater. Sci. **6**, 15 (1996).

[38] G. Kresse and J. Furthmüller, Efficient iterative schemes for *ab initio* total-energy calculations using a plane-wave basis set, Phys. Rev. B **54**, 11169 (1996).

[39] P. E. Blöchl, Projector augmented-wave method, Phys. Rev. B **50**, 17953 (1994).

[40] J. P. Perdew, K. Burke, and M. Ernzerhof, Generalized gradient approximation made simple, Phys. Rev. Lett. **77**, 3865 (1996).

[41] P. E. Blöchl, O. Jepsen, and O. K. Andersen, Improved tetrahedron method for Brillouin-zone integrations, Phys. Rev. B **49**, 16223 (1994).

[42] A. I. Liechtenstein, V. I. Anisimov, and J. Zaanen, Density-functional theory and strong interactions: Orbital ordering in Mott-Hubbard insulators, Phys. Rev. B **52**, R5467(R) (1995).

[43] H. Yu, C. Xu, X. Li, F. Lou, L. Bellaiche, Z. Hu, X. Gong, and H. Xiang, Complex spin Hamiltonian represented by an artificial neural network, Phys. Rev. B **105**, 174422 (2022).

[44] S. Toth and B. Lake, Linear spin wave theory for single-Q incommensurate magnetic structures, J. Phys.: Condens. Matter **27**, 166002 (2015).

[45] A. P. Thompson, H. M. Aktulga, R. Berger, D. S. Bolintineanu, W. M. Brown, P. S. Crozier, P. J. in't Veld, A. Kohlmeyer, S. G. Moore, T. D. Nguyen *et al.*, LAMMPS-a flexible simulation tool for particle-based materials modeling at the atomic, meso, and continuum scales, Comput. Phys. Commun. **271**, 108171 (2022).

[46] A. V. Ivanov, V. M. Uzdin, and H. Jónsson, Fast and robust algorithm for energy minimization of spin systems applied in

an analysis of high temperature spin configurations in terms of skyrmion density, Comput. Phys. Commun. **260**, 107749 (2021).

[47] J. Milano and M. Grimsditch, Magnetic field effects on the NiO magnon spectra, Phys. Rev. B **81**, 094415 (2010).

[48] M. J. Massey, N. H. Chen, J. W. Allen, and R. Merlin, Pressure dependence of two-magnon Raman scattering in NiO, Phys. Rev. B **42**, 8776(R) (1990).

[49] E. Aytan, B. Debnath, F. Kargar, Y. Barlas, M. M. Lacerda, J. X. Li, R. K. Lake, J. Shi, and A. A. Balandin, Spin-phonon coupling in antiferromagnetic nickel oxide, Appl. Phys. Lett. **111**, 252402 (2017).

[50] P. Fischer, M. Polomska, I. Sosnowska, and M. Szymanski, Temperature dependence of the crystal and magnetic structures of $BiFeO_3$, J. Phys. C: Solid State Phys. **13**, 1931 (1980).

[51] C. Ederer and N. A. Spaldin, Weak ferromagnetism and magnetoelectric coupling in bismuth ferrite, Phys. Rev. B **71**, 060401(R) (2005).

[52] D. Albrecht, S. Lisenkov, W. Ren, D. Rahmedov, I. A. Kornev, and L. Bellaiche, Ferromagnetism in multiferroic $BiFeO_3$ films: A first-principles-based study, Phys. Rev. B **81**, 140401(R) (2010).

[53] B. Xu, S. Meyer, M. J. Verstraete, L. Bellaiche, and B. Dupé, First-principles study of spin spirals in the multiferroic $BiFeO_3$, Phys. Rev. B **103**, 214423 (2021).

[54] G. Vignale and W. Kohn, Current-dependent exchange-correlation potential for dynamical linear response theory, Phys. Rev. Lett. **77**, 2037 (1996).

[55] Z. Qian and G. Vignale, Dynamical exchange-correlation potentials for an electron liquid, Phys. Rev. B **65**, 235121 (2002).

[56] T. Gilbert, A phenomenological theory of damping in ferromagnetic materials, IEEE Trans. Magn. **40**, 3443 (2004).

[57] A. Kumar, C. J. Fennie, and K. M. Rabe, Spin-lattice coupling and phonon dispersion of $CdCr_2O_4$ from first principles, Phys. Rev. B **86**, 184429 (2012).

[58] X. Wu, Z. Liu, and T. Luo, Magnon and phonon dispersion, lifetime, and thermal conductivity of iron from spin-lattice dynamics simulations, J. Appl. Phys. **123**, 085109 (2018).

[59] J. Hellsvik, D. Thonig, K. Modin, D. Iuşan, A. Bergman, O. Eriksson, L. Bergqvist, and A. Delin, General method for atomistic spin-lattice dynamics with first-principles accuracy, Phys. Rev. B **99**, 104302 (2019).

[60] K. L. Merkle and D. J. Smith, Atomic structure of symmetric tilt grain boundaries in NiO, Phys. Rev. Lett. **59**, 2887 (1987).

[61] L. Li, L. Chen, R. Qihe, and G. Li, Magnetic crossover of NiO nanocrystals at room temperature, Appl. Phys. Lett. **89**, 134102 (2006).

[62] G. Henkelman, B. P. Uberuaga, and H. Jónsson, A climbing image nudged elastic band method for finding saddle points and minimum energy paths, J. Chem. Phys. **113**, 9901 (2000).

[63] J. M. Munro, H. Akamatsu, H. Padmanabhan, V. S. Liu, Y. Shi, L.-Q. Chen, B. K. VanLeeuwen, I. Dabo, and V. Gopalan, Discovering minimum energy pathways via distortion symmetry groups, Phys. Rev. B **98**, 085107 (2018).

[64] F. Zavaliche, P. Shafer, R. Ramesh, M. P. Cruz, R. R. Das, D. M. Kim, and C. B. Eom, Polarization switching in epitaxial $BiFeO_3$ films, Appl. Phys. Lett. **87**, 252902 (2005).

[65] J. Heron, J. Bosse, Q. He, Y. Gao, M. Trassin, L. Ye, J. Clarkson, C. Wang, J. Liu, S. Salahuddin *et al.*, Deterministic switching of ferromagnetism at room temperature using an electric field, Nature (London) **516**, 370 (2014).

[66] J. Chen and S. Dong, Manipulation of magnetic domain walls by ferroelectric switching: Dynamic magnetoelectricity at the nanoscale, Phys. Rev. Lett. **126**, 117603 (2021).